Bipolarons from long-range interactions: Singlet and triplet pairs in the screened Hubbard-Fröhlich model on the chain

J. P. Hague[1] and P. E. Kornilovitch[2]
[1]*Department of Physics and Astronomy, The Open University, Walton Hall, Milton Keynes MK7 6AA, United Kingdom*
[2]*Hewlett-Packard Company, 1000 NE Circle Boulevard, Corvallis, Oregon 97330, USA*
(Received 23 April 2009; published 3 August 2009)

We present details of a continuous-time quantum Monte Carlo algorithm for the screened Hubbard-Fröhlich bipolaron. We simulate the bipolaron in one dimension with arbitrary interaction range in the presence of Coulomb repulsion, computing the effective mass, binding energy, total number of phonons associated with the bipolaron, mass isotope exponent, and bipolaron radius in a comprehensive survey of the parameter space. We discuss the role of the range of the electron-phonon interaction, demonstrating the evolution from Holstein to Fröhlich bipolarons and we compare the properties of bipolarons with singlet and triplet pairing. Finally, we present simulations of the bipolaron dispersion. The bandwidth of the Fröhlich bipolaron is found to be broad and the decrease in bandwidth as the two polarons bind into a bipolaron is found to be far less rapid than in the case of the Holstein interaction. The properties of bipolarons formed from long-range electron-phonon interactions, such as light strongly bound bipolarons and intersite pairing when Coulomb repulsion is large, are found to be robust against screening, with qualitative differences between Holstein and screened Fröhlich bipolarons found even for interactions screened within a single lattice site.

DOI: 10.1103/PhysRevB.80.054301 PACS number(s): 71.38.Mx, 71.38.Fp, 71.10.Fd

I. INTRODUCTION

Electron-phonon interactions have significant effects in quasi-one-dimensional solids and can lead to the formation of polarons. As shown by angle-resolved photoemission spectroscopy, the quasiparticles of the one-dimensional cuprate $SrCuO_2$ (Ref. 1) and the conductor $K_{0.3}MoO_3$ (Ref. 2) are significantly modified by interactions with phonons. Strong electron-phonon interactions are also expected to be relevant in low-dimensional organic semiconductors.[3] The large phonon-mediated attractions in low-dimensional materials may also lead to pairing of polarons into bipolarons. In one-dimensional (1D) systems, bipolarons can have either singlet or triplet symmetry and the presence of triplet bipolarons has been observed in disordered conducting polymers using electron-spin-resonance measurements.[4] It is the purpose of this paper to present a comprehensive set of simulations of the properties of 1D bipolarons that are bound with long-range electron-phonon coupling.

The polaron problem was originally formulated by Landau[5] to describe the effects of lattice polarization on the properties of electrons. As an electron moves through a material, it polarizes the underlying medium of ions and electrons leading to a dipole field and thus an electron-phonon interaction. Typically the interaction causes a cloud of phonons to follow a single electron and the combination of the particles is called a polaron. The mass of polarons may be significantly larger than that of the individual electrons.[6] It is now well established that polarons are formed in many materials and are probably one of the most common excitations in the solid state.

More controversial is the existence of bound pairs of polarons known as bipolarons. If the electron-phonon interaction is sufficiently attractive, then it is possible for two polarons to pair.[7] It is necessary that phonon-mediated attraction must overcome the inherent Coulomb repulsion between electrons in order for the pair to form. Studies of the continuum limit of the bipolaron have shown that bipolaron may be stable but only in a very small region of the parameter space of retarded attraction and Coulomb repulsion.[8]

With the goal of understanding the properties of bipolarons, we have developed a quantum Monte Carlo technique for numerically exact simulation of two electrons interacting via both Coulomb repulsion and phonon-mediated attraction.[6,9] Our approach is formulated in continuous time and therefore has the advantage that there are no finite-size effects from the Trotter decomposition. We are also able to examine very large lattices and to consider general long-range forms for the electron-phonon problem. Properties of the short-range Hubbard-Holstein bipolaron were studied using quantum Monte Carlo[10,11] and exact diagonalization on small lattices.[12,13] In 1D, the ground-state properties of bipolarons forming through local and nearest-neighbor interactions can be found using an advanced variational technique which predicted that long-range electron-phonon interactions may lead to light pairs in 1D.[14,15] We have subsequently determined that bipolarons interacting via very long-range attractive potentials on triangular lattices may be exceptionally light.[9,16]

Our algorithm can compute numerically exact bipolaron dispersions. Previously, dispersions of the Hubbard-Holstein model have been computed on small lattices, using exact-diagonalization techniques at relatively strong coupling[12] and using an optimized phonon approach for exact diagonalization at weak couplings.[13] Long-range interactions were also studied on small lattices.[17] The intermediate coupling dispersions of a modified Hubbard-Holstein model have been computed using an approximate variational technique.[18] In principle, approximate dispersions could also be extracted from the spectral functions in Ref. 10. Bipolaron dispersions computed by ElShawish for the Hubbard-Holstein model using the same method as in Ref. 19 were also presented in Ref. 10.

Our aim here is to simulate the singlet and triplet pairs that form in systems described by a generic Hubbard-Fröhlich Hamiltonian with local Coulomb repulsion and long-range electron-phonon interaction.[20] A crucial feature of this model Hamiltonian is that it treats both strong electronic repulsion and attraction from electron-phonon interaction on equal footing. The Hamiltonian has the following form

$$H = -t\sum_{\langle nn'\rangle\sigma} c^{\dagger}_{n'\sigma}c_{n\sigma} + \sum_{nn'\sigma}\frac{V(\boldsymbol{n},\boldsymbol{n}')}{2}c^{\dagger}_{n\sigma}c_{n\sigma}c^{\dagger}_{n'\bar{\sigma}}c_{n'\bar{\sigma}} + \sum_{m}\frac{\hat{P}^2_m}{2M} + \sum_{m}\frac{\xi^2_m M\omega^2}{2} - \sum_{nm\sigma} f_m(\boldsymbol{n})c^{\dagger}_{n\sigma}c_{n\sigma}\xi_m.$$

Each ion has a displacement ξ_m. Sites labels are $\boldsymbol{n}$ or $\boldsymbol{m}$ for electrons and ions, respectively. c operators annihilate electrons. The phonons are Einstein oscillators with frequency ω and mass M. $\langle \boldsymbol{nn}'\rangle$ denote pairs of nearest-neighbor sites and $\hat{P}_m$ are the momentum operators of the ions. The instantaneous interaction $V(\boldsymbol{n},\boldsymbol{n}')$ has an on-site component U which we always treat as repulsive and an off-site component V. We consider three forms for the electron-ion force function, f. The Holstein interaction is $f_m(\boldsymbol{n})=\kappa\delta_{nm}$, leading to a Hubbard-Holstein model. The near-neighbor model introduced by Bonča and Trugman has the form $f_m(\boldsymbol{n})=\kappa[\delta_{n,m+1/2}+\delta_{n,m-1/2}]/2$. The Fröhlich interaction force is long range, $f_m(\boldsymbol{n})=\kappa[(\boldsymbol{m}-\boldsymbol{n})^2+1]^{-3/2}\exp(-|\boldsymbol{m}-\boldsymbol{n}|/R_{sc})$, where κ is a constant and R_{sc} is the screening radius. It is useful to introduce the dimensionless constant $\lambda=\kappa^2/2M\omega^2W$ (polaron shift normalized by the half bandwidth, $W=2t$) which characterizes the strength of the electron-phonon coupling.

The Lang-Firsov transformation can be used to understand the extreme antiadiabatic limit of electron-phonon models, mapping onto a Hubbard-type system with instantaneous interaction between electrons.[21] The Hubbard-Holstein model maps directly to a Hubbard model with a new interaction $\tilde{U}=U-2W\lambda$. Since pairs are bound in 1D for any attractive interaction, the critical lambda for singlet formation is $\lambda_C=U/2W$.

In the antiadiabatic limit, the near-neighbor model becomes a UV model with $\bar{U}=U-2W\lambda$ and $\bar{V}=2W\lambda\phi(\boldsymbol{a})$. The near-neighbor model may be solved analytically to determine the binding condition $\bar{V}>2\bar{U}t/(\bar{U}+4t)$ for singlet and $\bar{V}>2t$ for triplet pairing[22] [we use the symbols $\bar{U}$ and $\bar{V}$ when discussing the UV model to distinguish from the U in Eq. (1)]. Singlet and triplet pairs are degenerate for very large U. Since the wave function of triplet states has a node at zero separation, triplet states do not depend on U. The high-phonon frequency limit of the Fröhlich model has a long-range instantaneous attractive tail, which makes determination of the binding condition quite complicated.[23] Here, we will investigate bound states for finite phonon frequencies.

A feature of the models with long-range electron-phonon interaction is that several different configurations of bipolarons can pair. Bipolarons may be of a singlet type, strongly bound into an on-site pair denoted S0, or an intersite pair separated by one lattice site denoted S1, which has a zero in the pair wave function for zero separation. Triplets are never formed in the Hubbard-Holstein model but are permitted in the models with long-range interaction.

This paper is organized as follows: the continuous-time quantum Monte Carlo algorithm for bipolarons is outlined in Sec. II. In Secs. III and IV, we simulate singlet and triplet bipolaron properties. Dispersions and densities of states are presented in Sec. V. We summarize in Sec. VI. The Appendix contains complete details of the Monte Carlo algorithm.

II. ALGORITHM

The continuous-time quantum Monte Carlo algorithm for bipolarons is an extension of a similar path-integral method for simulating the polaron.[6] An integration over phonon degrees of freedom leads to an effective action. In the two-particle case, the action is a functional of two polaron paths in imaginary time,[16]

$$\begin{aligned}A[\boldsymbol{r}(\tau)] = {} & \frac{z\lambda\bar{\omega}}{2\Phi_0(0,0)}\int_0^{\bar{\beta}}\int_0^{\bar{\beta}} d\tau d\tau' e^{-\bar{\omega}\bar{\beta}/2}(e^{\bar{\omega}(\bar{\beta}/2-|\tau-\tau'|)} \\ & + e^{-\bar{\omega}(\bar{\beta}/2-|\tau-\tau'|)})\sum_{ij}\Phi_0[\boldsymbol{r}_i(\tau),\boldsymbol{r}_j(\tau')] \\ & + \frac{z\lambda\bar{\omega}}{\Phi_0(0,0)}\int_0^{\bar{\beta}}\int_0^{\bar{\beta}} d\tau d\tau' e^{-\bar{\omega}\tau}e^{-\bar{\omega}(\bar{\beta}-\tau')} \\ & \times\sum_{ij}(\Phi_{\Delta r}[\boldsymbol{r}_i(\tau),\boldsymbol{r}_j(\tau')] - \Phi_0[\boldsymbol{r}_i(\tau),\boldsymbol{r}_j(\tau')]) \\ & - \int_0^{\beta} V[\boldsymbol{r}_1(\tau),\boldsymbol{r}_2(\tau)]d\tau. \end{aligned} \quad (1)$$

The retarded interaction mediated by the phonons is characterized by $\Phi_{\Delta r}[\boldsymbol{r}(\tau),\boldsymbol{r}(\tau')]=\Sigma_m f_m[\boldsymbol{r}(\tau)]f_{m+\Delta r}[\boldsymbol{r}(\tau')]$, where the vector $\Delta\boldsymbol{r}=\boldsymbol{r}(\beta)-\boldsymbol{r}(0)$ is an offset between the end configurations. $\Delta\boldsymbol{r}$ enables the computation of momentum-dependent properties[6] and is schematically introduced in Fig. 1. The indices i and $j=1,2$ denote which fermion path is being considered. The dimensionless variables $\bar{\omega}=\hbar\omega/t$ and $\bar{\beta}=t/k_BT$. An instantaneous Coulomb repulsion, $V[\boldsymbol{r}_1,\boldsymbol{r}_2]$, is also included. The weight of a configuration is given by $\exp(A)$.

Our electron paths are continuous in time with hops between sites (kinks) introduced or removed from the path on each Monte Carlo step. In contrast to the one-particle algorithm, kinks and antikinks must be updated in pairs to maintain boundary conditions in imaginary time. Another significant difference between one-particle and two-particle algorithms is particle exchange, leading to bipolarons with singlet and triplet symmetries. Measurements of the ground-state singlet bipolaron are not subject to sign problems. It is also interesting to measure the properties of triplet bipolarons, which depend on the sign that the wave function picks up under exchange. Estimators for the triplet bipolaron will be discussed later.

We use a correlated weighting scheme for kink addition and removal, and a simple weighting scheme for path selec-

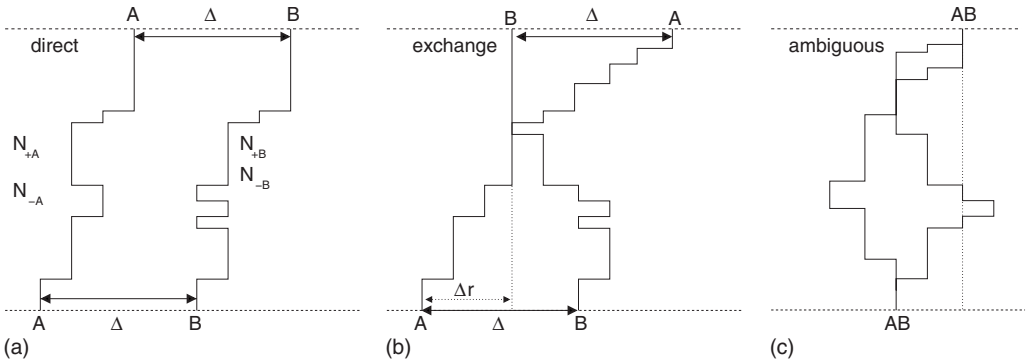

FIG. 1. Example paths in 1D, showing the notation and concepts of the bipolaron simulation. (a) Paths in the direct configuration. The ends of the paths are separated by a distance Δ. There are N_{+A} kinks and N_{-A} antikinks on the first path and equivalent numbers for the second (B) path. (b) In the exchanged configuration, the paths cross. A feature of the 1D problem is that there is always at least one shared segment between kinks in the exchanged configuration. Thus if the Coulomb repulsion is infinite, there can be no exchanged configuration. (c) There is a third configuration where the endpoints of the paths sit on the same site, which we call the ambiguous configuration. When the singlet properties are calculated, all path configurations are associated with a factor 1. For triplet properties, direct configurations have a sign 1, exchanged a sign −1, and ambiguous have sign 0.

tion and kink type. (R1) Choose a kink with direction (type) $\boldsymbol{l}$ from all possible hops with equal probability $P_{\boldsymbol{l}}=1/N_k$ and determine the antikink as $-\boldsymbol{l}$. N_k is the number of possible hops between sites (normally the number of nearest neighbors). $P_{\boldsymbol{l}}$ always cancels in the balance equations. (R2) Assign path A with probability 1/2 from both paths and assign path B as the other path. (R3) Choose shift type for the first kink with equal probability $P_S=1/2$. There are two shift types, the path above the kink insertion point can be shifted through $\boldsymbol{l}$ or the path below the insertion point can be shifted through $-\boldsymbol{l}$. (R4) When selecting the first kink to remove (which has type $\boldsymbol{l}$), we do so with probability $1/N_{A\boldsymbol{l}}(I)$. Where I is the configuration before removal. That kink is at time τ. (R5) When selecting the second kink of type $\boldsymbol{l}$ to remove from path A, we do so with probability $p(\tau',\tau)/\Sigma_{i=1}^{N_{A\boldsymbol{l}}(I)}p(\tau_i,\tau)$. Where I is the configuration before removal. (R6) Always insert the first kink at τ with probability density $p(\tau)=1/\beta$. (R7) Always insert the second kink at τ' with probability $p(\tau',\tau)$. (R8) Choose shift type for kink 2 from kink 1, depending if shifts are correlated (no change in interpath distance) or anticorrelated.

The probability $p(\tau',\tau)$ can be chosen either as unity, recovering previous insertion and removal rules,[9] or $p(\tau',\tau)$ can be larger for kinks that are separated by smaller time differences, potentially leading to improved acceptance ratios at strong coupling. We use the weighting $p(\Delta\tau)=\theta(\alpha-\Delta\tau)/2\alpha+1/2\beta$, where θ is the step function and α is a parameter that can be made smaller to improve acceptance ratios ($\Delta\tau=\tau'-\tau$ is mapped onto the interval $[0,\beta)$ and $0<\alpha<\beta$).

In the two-particle case, it is necessary to operate on two kinks simultaneously to ensure that the end configurations of the paths satisfy the boundary conditions. We have previously discussed how the algorithm works without exchange (applicable to ladder systems where particles sit on different legs). Four extra Monte Carlo update rules can be used in the exchanged configuration, bringing the potential number of binary updates to eight. The new rules are required to ensure ergodicity in the exchanged configuration. Here we summarize all the possible updates: (I) two kinks of the same type $\boldsymbol{l}$ are added to (or removed from) two different paths. (II) A kink-antikink pair is added to (or removed from) one of the two paths. (III) A kink of type $\boldsymbol{l}$ is inserted into one path and another kink of the same type $\boldsymbol{l}$ is removed from the same path. This type of update shifts kinks in imaginary time. It is not essential. (IV) A kink of type $\boldsymbol{l}$ is added to one path and an antikink $-\boldsymbol{l}$ is removed from the other path (this is also not essential). (V) Addition (or removal) of kink $\boldsymbol{l}$ and antikink $-\boldsymbol{l}$ on different paths. (VI) Kink type $\boldsymbol{l}$ is inserted on one path and kink type $\boldsymbol{l}$ is removed from the other. (VII) Addition of kink $\boldsymbol{l}$ and removal of antikink $-\boldsymbol{l}$ on the same path. (VIII) Addition (or removal) of a pair of kinks of type $\boldsymbol{l}$ on a single path.

In the direct configuration, updates (I–IV) may be used and the shift types of the two kinks may be identical (correlated) or opposite (anticorrelated). It is convenient to think of the separate correlated and anticorrelated updates as eight different updates. In the exchanged configuration, updates (I–IV) are used unchanged, except that the shifts on both paths must be correlated (i.e., both top or both bottom) to maintain the correct boundary conditions in time, thus I–IV only count as four updates. The remaining four updates (V–VIII) are used only with anticorrelated shifts, thus in total, there are eight possible updates in the exchanged configuration. Updates (V–VIII) are essential to access the whole configuration space as they change the interpath distance $\boldsymbol{\Delta}$ of the exchanged configuration. Finally in the ambiguous configuration, all the possible updates may be used. To simplify the scheme and its testing, we use a minimal update set of I, II, V, and VIII. Details of the probabilities for binary updates are given in the Appendix.

The algorithm can be made more efficient by introducing Monte Carlo updates to change the paths from direct into exchanged configurations. In the path-integral formalism, an exchange of particles corresponds to swapping the ends of the paths at $\tau=\beta$. An example of an exchanged configuration is shown in Fig. 1. To make the exchange in 1D, the $\tau=\beta$ end of path B must be shifted by $-\Delta$ lattice sites and that of path

A through $+\Delta$ sites. This can be achieved by inserting $\Delta-n$ kinks and removing n antikinks from path A, and inserting $\Delta-m$ antikinks and removing m kinks from path B. Details of how to take the continuous-time limit of this type of update are provided in the Appendix. This kind of exchange update is relatively slow and we attempt this with a small probability on the order of 10% on any Monte Carlo step.

There is another way of carrying out exchange updates. If the paths occupy the same lattice site at the same point in imaginary time, then the paths have a segment in common. The paths can be broken at that segment with the bottom of path A attached to the top of path B and the bottom of path B to the top of path A. This type of exchange can speed up the computation of triplet properties since the update is very fast and it can be attempted regularly without loss of speed. In our algorithm, we attempt a common segment exchange with probability p_{CS} every time an exchange is attempted. Once the attempt is started, we test for the existence of a common segment. If there are no shared segments, then the update is rejected and no further update is attempted on that Monte Carlo step. Otherwise, the common segment exchange is accepted with probability $P(C\rightarrow D)=\min\{1,\exp[A(D)-A(C)]\}$.

There is another update that can be useful if the action has a similar value for path configurations with small and large separation (as is typically the case when the bipolaron is only just bound). Then it can be appropriate to attempt to shift one of the paths through a longer distance when the paths are in a direct configuration. This update enables more rapid sampling of the path configurations and is especially useful for making accurate measurements of the interparticle separation.

After a warm-up period, we make a series of measurements. The measurements are made every few updates to avoid correlation between Monte Carlo steps. We also use a blocking procedure in conjunction with bootstrap resampling for error estimation. In situations where the measurements take a long time (comparable with the computation of the action)—such as the estimators for the total energy and isotope exponent, this sparse sampling acts to speed up the algorithm since correlated measurements do not improve estimation of the averages.

Estimators relevant to the current paper are the total singlet energy,

$$E=-\lim_{\beta\rightarrow\infty}\left[\left\langle\frac{\partial A}{\partial\beta}\right\rangle+\frac{1}{\beta}\left\langle\sum_i N_i\right\rangle\right], \tag{2}$$

where N_i is the number of kinks of type i and angular brackets denote ensemble averaging. The number of phonons associated with the bipolaron,

$$N_{\mathrm{ph}}=-\lim_{\beta\rightarrow\infty}\frac{1}{\bar{\beta}\langle s\rangle}\left\langle s\ \left.\frac{\partial A}{\partial\bar{\omega}}\right|_{\lambda\bar{\omega}}\right\rangle, \tag{3}$$

where the derivative is taken keeping $\lambda\bar{\omega}$ constant. $s=1$ when considering singlet states and $s=1,0,-1$ for measurements of triplet states, as described in Fig. 1. The bipolaron band energy spectrum can be computed from

$$\epsilon(\boldsymbol{k})-\epsilon(0)=-\lim_{\beta\rightarrow\infty}\frac{1}{\beta}\ln\left(\frac{\langle s\cos(\boldsymbol{k}\cdot\Delta\boldsymbol{r})\rangle}{\langle s\rangle}\right), \tag{4}$$

where $\mathbf{k}$ is the quasimomentum. By expanding this expression in small $\mathbf{k}$, the ith component of the inverse effective mass is found to be

$$\frac{1}{m_i^*}=\lim_{\beta\rightarrow\infty}\frac{1}{\beta\hbar^2}\frac{\langle s(\Delta\boldsymbol{r}_i)^2\rangle}{\langle s\rangle}. \tag{5}$$

We compute the bipolaron radius as the root-mean-square distance between paths,

$$R_{bp}=\frac{1}{\langle s\rangle}\left\langle s\sqrt{\frac{1}{\beta}\int_0^\beta[\boldsymbol{r}(\tau)_1-\boldsymbol{r}(\tau)_2]^2d\tau}\right\rangle. \tag{6}$$

The mass isotope coefficient, $\alpha_{m_i^*}=d\ln m_i^*/d\ln M$, is calculated as follows:

$$\alpha_{m_i^*}=\lim_{\beta\rightarrow\infty}\frac{\bar{\omega}}{2}\frac{1}{\langle s(\Delta\boldsymbol{r}_i)^2\rangle}\times\left[\left\langle s(\Delta\boldsymbol{r}_i)^2\ \left.\frac{\partial A}{\partial\bar{\omega}}\right|_\lambda\right\rangle-\frac{\langle s(\Delta\boldsymbol{r}_i)^2\rangle}{\langle s\rangle}\left\langle s\ \left.\frac{\partial A}{\partial\bar{\omega}}\right|_\lambda\right\rangle\right]. \tag{7}$$

The singlet-triplet splitting can also be determined,

$$\Delta_{st}=-\frac{1}{\beta}\ln(\langle s\rangle). \tag{8}$$

Since $\langle s\rangle$ is always less than 1, the singlet-triplet splitting is always positive and the energy of the triplet state is higher in energy, as expected since the ground-state wave function of two particles should have no nodes.

An alternative way of computing spectra and density of states is also available. We take the measurement $\langle\delta_{\boldsymbol{r},\Delta\boldsymbol{r}}\rangle$ for values of $\boldsymbol{r}$ consistent with a few lattice spacings. The magnitude of the measurement drops off very rapidly with $\boldsymbol{r}$. Then the whole spectrum can be computed for any $\boldsymbol{k}$ point without deciding which $\boldsymbol{k}$ to investigate before the algorithm starts. The expression for the dispersion calculated in this way is

$$\epsilon_{\boldsymbol{k}}-\epsilon_0=-\ln\left(\sum_{\boldsymbol{r}}\cos(\boldsymbol{k}\,.\,\boldsymbol{r})\frac{\langle s\,\delta_{\boldsymbol{r},\Delta\boldsymbol{r}}\rangle}{\langle s\rangle}\right)/\beta. \tag{9}$$

This form is particularly useful for determining the density of bipolaron states.

In the following, we have restricted the electron paths to remain within 200 lattice sites of each other by enforcing a pairwise infinite instantaneous potential well dependent on the interparticle separation. This stops paths from moving apart indefinitely. The 200-site well is sufficiently large to ensure that finite-size effects are negligible compared with other considerations such as the statistical error in the Monte Carlo averaging. We note that to obtain accurate results, we require that the inverse temperature is at least $\beta\sim 14/\omega$. Since the number of kinks in the paths increases with β and the computation time for the action scales as the square of the number of kinks, this limits practical computation to

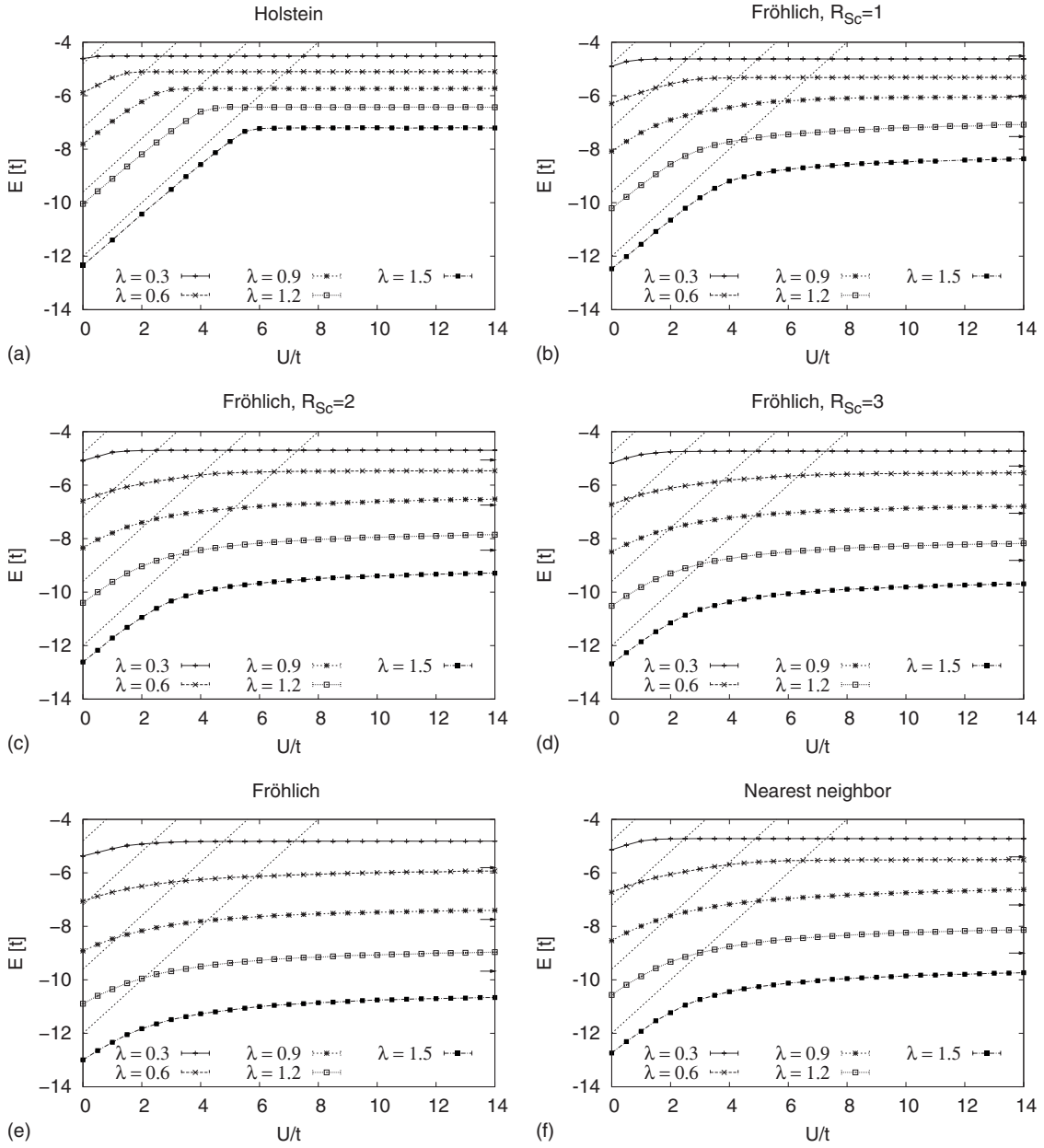

FIG. 2. Total energy associated with the singlet bipolaron for the three different models. The limits corresponding to strongly bound S0 bipolarons are shown as dotted lines and arrows on the right axis correspond to strongly bound S1 bipolarons. The surprising result here is that the long-range tails in the Hubbard-Fröhlich model with $R_{sc}=3$ lead to similar results to the near-neighbor model proposed by Bonča and Trugman. In the results for the Hubbard-Holstein model, there is a sudden change in the gradient of the plot around the critical coupling. This is not apparent for either of the models with long-range coupling. $\bar{\beta}=14$ in all figures in this section.

$\omega/t>1$ or $\omega/W>1/2$. Thus our calculations reach just inside the adiabatic regime.

III. SINGLET BIPOLARON

In this section, we examine and compare the properties of the singlet bipolarons formed in the Hubbard-Holstein model, screened and unscreened Hubbard-Fröhlich models, and in the nearest-neighbor model. We compute the total energy, inverse mass, inverse radius, mass isotope exponent, and number of phonons associated with the bipolaron cloud.

We begin by examining the total energy associated with the singlet bipolaron, which can be seen in Fig. 2. The energy is plotted for a range of U/t and λ with fixed $\bar{\omega}=1$. In the Hubbard-Holstein model, there is a rapid change in the gradient of the plot around the critical coupling for binding (for large U, the graph is flat because the two polarons are not bound and so do not interact through the local U). The long-range tails in the screened Hubbard-Fröhlich model with $R_{sc}=3$ lead to energies that are similar to the near-neighbor model and the difference in energies is barely detectable by eye. This is a strong indicator that the nearest-neighbor interaction strength $\Phi(\boldsymbol{a})$ is the most important

factor in determining the properties of the bipolaron. $\Phi(\boldsymbol{a})=0.5$ in the near-neighbor model and $\Phi(\boldsymbol{a})=0.4688$ to four significant figures in the $R_{sc}=3$ screened Fröhlich model (where $\boldsymbol{a}$ is the lattice vector). The unscreened Fröhlich interaction leads to bipolarons that are more strongly bound. For example, a much larger U/t is needed to unbind the bipolaron when the Fröhlich interaction is simulated at $\lambda=0.3$. In the limit of low-screening radius, the energy of the bipolaron approaches the Holstein limit very slowly, with the very rapid binding close to a critical U associated with the Holstein model not seen in models with long-range interaction. This is a qualitative difference between Holstein models and those with a small amount of intersite attraction.

In the very strongly bound limit, the effects of electron hopping are small. An effective atomic Hamiltonian can be found by applying the Lang-Firsov transformation to the phonon part of the Hamiltonian,

$$\tilde{H}_{\mathrm{at}}=-\sum_{ii'}\frac{2t\lambda\Phi_0(i,i')}{\Phi_0(0,0)}n_in_{i'}+\omega\sum_j\left(d_j^{\dagger}d_j+\frac{1}{2}\right). \quad (10)$$

Reintroducing the effects of Coulomb repulsion, the total energy of the strongly bound on-site bipolaron (formed when $8t\lambda>U$) can be computed to be

$$E=U-8t\lambda. \quad (11)$$

The energy of the strongly bound S1 bipolaron at large λ and $U\gg 2t\lambda$ is

$$E=-4t\lambda[1+\Phi(\boldsymbol{a})/\Phi_0]. \quad (12)$$

These limits are also shown in Fig. 2 (the strong binding S1 energies are only shown for $\lambda=0.9$, 1.2, and 1.5). There is a clear convergence between the numerics and the strongly bound S0 state at low U. Bipolarons with long-range interactions converge on the limit more slowly than Holstein bipolarons. The S1 energies at large U begin to agree at large λ. This is expected since the bipolarons formed in models with long-range interactions are quite mobile, so the effects of hopping should be considered, even when $\lambda=1.5$. Note that there is no S1 bipolaron in the very large $U\gg 2t\lambda$ limit of the Holstein model.

The total number of phonons associated with the singlet bipolaron is shown in Fig. 3. The similarity between the pairs in the models with long-range interaction and the distinction with the Holstein bipolaron is clearly visible. The near-neighbor and lattice-Fröhlich models show only quantitative differences. In particular, the crossover between weakly and strongly bound cases in the models with long-range interaction is gentle in comparison with that seen in the Hubbard-Holstein model; in the case of the Holstein interaction the bipolaron is rapidly bound on decreasing U, causing an abrupt increase in the number of phonons associated with the bipolaron.

The total number of phonons associated with the strongly bound on-site bipolaron (following the argument in Ref. 9) is

$$N_{\mathrm{ph}}=\frac{8\lambda}{\bar{\omega}}. \quad (13)$$

Note that the number of phonons in the strongly bound on-site bipolaron does not depend on U, so the number of phonons reaches a limiting value on decreasing U. This limit can be seen in Fig. 3 as the arrows on the left-hand y axis. The Holstein bipolaron rapidly approaches the strongly bound S0 limit on decreasing U with the S0 limit approached less rapidly as R_{sc} increases. The reason for this is that the longer range tails lead to a shallower effective potential, so S0 bipolarons are harder to bind into purely on-site pairs. The number of phonons associated with the S1 bipolaron can also be found,

$$N_{\mathrm{ph}}=\frac{4t\lambda}{\omega}[1+\Phi(\boldsymbol{a})/\Phi_0]. \quad (14)$$

This is represented as arrows on the right-hand side of the graphs. Again it is clear that hopping effects should be included at intermediate λ, with the agreement becoming better as λ is increased and the bipolaron becomes more strongly bound.

We show the inverse mass of the singlet bipolaron in Fig. 4. Both the more complicated Hubbard-Fröhlich bipolaron and the simplified model with only nearest-neighbor interaction generate bipolarons with similar light mass. At large U, the mass of the Holstein bipolaron does not change because the bipolaron is not bound. This is also true of the long-range models at small enough λ. There is a notable feature in the mass at intermediate $U\sim 3$ and $\lambda=1.5$. The mass associated with the nearest-neighbor bipolaron has a hump, with the bipolaron becoming lighter on increasing U, before becoming slightly heavier again.

We have not been able to compute analytical expressions for the mass in the strong-coupling limit of the Hubbard-Fröhlich model since each electron hop excites phonons at an infinite number of sites, complicating the second-order perturbation theory. For the near-neighbor and Holstein models, the strong binding limits have been discussed by Bonča and Trugman.[14,15] As noted by Bonča and Trugman,[15] the energies of S0 and S1 configurations in the near-neighbor model with high phonon frequency are degenerate when $U=W\lambda$ at large ω. This also occurs in the Hubbard-Fröhlich model when $U-2W\lambda=2W\lambda\phi(\boldsymbol{a})$. At this point, the motion of the bipolarons is first order in t since the electron does not need to tunnel through a high energy barrier to move, leading to the mass decrease that can be seen in Fig. 4. In this sense, the mass decrease is similar in origin to the superlight small bipolarons seen on lattices with a triangular component.[9] The decrease in mass at intermediate U is less pronounced in the case of the unscreened Fröhlich interaction, and not visible to the eye on the plot, but is present with a peak at around $U/t=4$ for the $\lambda=1.5$ plot.

The pair size associated with the singlet bipolaron (shown in Fig. 5) demonstrates the crossover between S0 and S1 bipolarons. There is a qualitative difference between models with short-range and long-range interactions. For larger electron-phonon couplings and long-range interactions, the

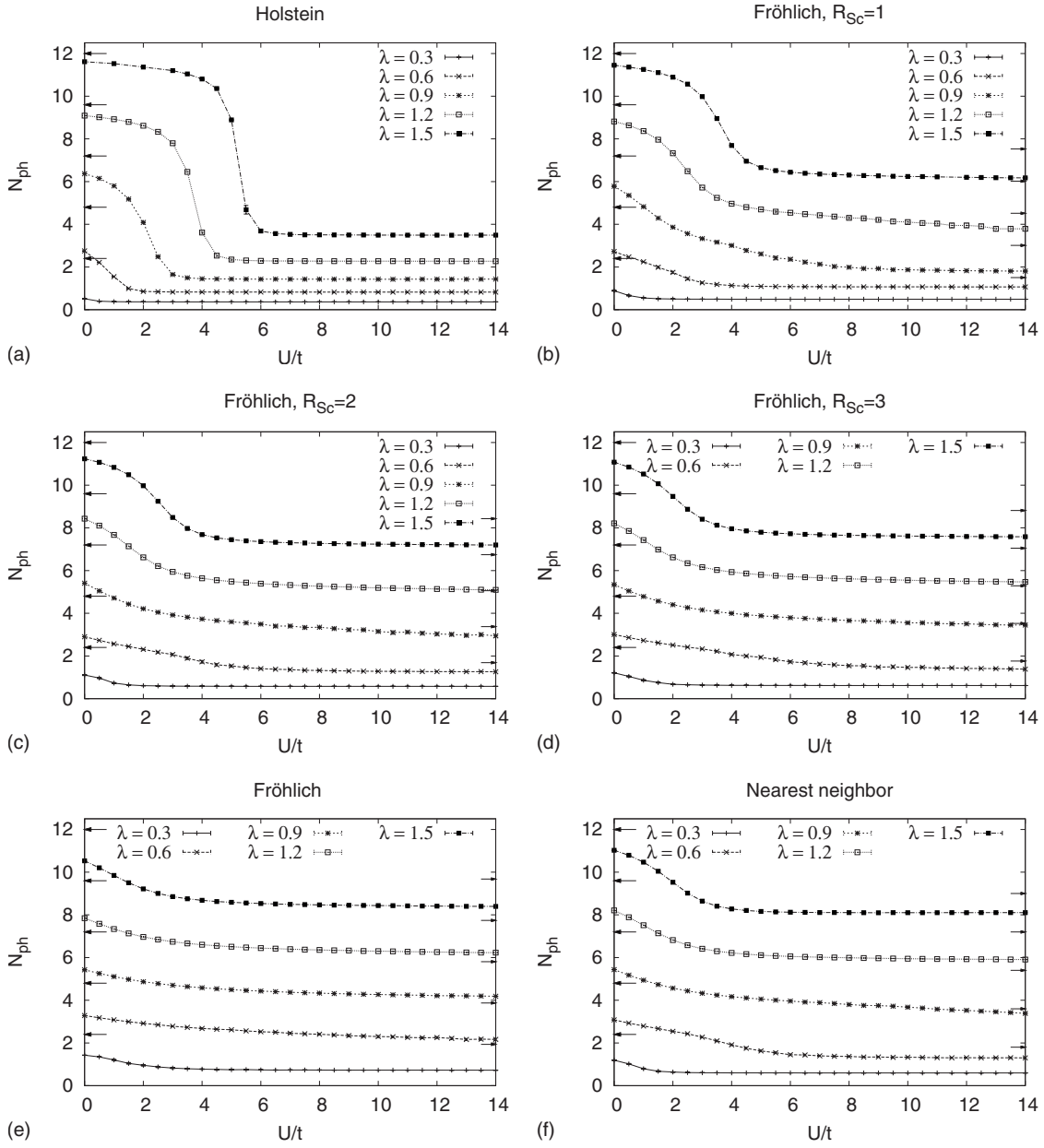

FIG. 3. Total number of phonons associated with the singlet bipolaron. The limits corresponding to strongly bound S0 bipolarons are shown as arrows on the left axis and arrows on the right axis correspond to strongly bound S1 bipolarons. The similarity between the two models with long-range interaction and the distinction with the Holstein bipolaron can immediately be seen. The nearest-neighbor and lattice-Fröhlich models show only quantitative differences. In particular, the crossover from the weakly to strongly bound states is gentle in comparison with the Holstein interaction, where the bipolaron is suddenly bound at a critical coupling, causing a sudden increase in the number of phonons associated with the bipolaron.

bipolaron size changes from small (on site) $R_{bp} < a$ to intersite $R_{bp} \sim a$ (the lattice constant) on increasing U. The change between these two types of bipolaron occurs at $U \sim 3$ for $\lambda = 1.5$ in the nearest-neighbor model. The pair size associated with the unscreened Fröhlich interaction is not as small as that for the screened Fröhlich interaction, presumably because the potential well does not change so rapidly with lattice index. It can be seen that at large U, the S1 bipolaron becomes more strongly bound on increasing λ with the inverse radius tending toward unity at $U = 14$. Again this demonstrates that the S1 bipolaron can only be considered to be strongly bound at large λ and $U \gg \lambda$. In contrast, the Holstein bipolaron is always unbound at large U, as the bipolaron radius becomes infinite ($R_{bp}^{-1} \to 0$). The modification of the binding diagram on changing R_{sc} can be seen in these figures. For $R_{sc} = 1$, $\lambda = 1.5$ is needed to bind the bipolaron at strong U, whereas the Fröhlich bipolaron binds at $\lambda = 0.9$.

We finish this section by computing the mass isotope exponent, α, which is plotted in Fig. 6 for a variety of λ and U. A dip in the isotope exponent seen in the nearest-neighbor and screened Fröhlich interactions corresponds to the hump seen in the inverse mass. Again, this dip coincides with the degeneracy in the S0 and S1 energies.

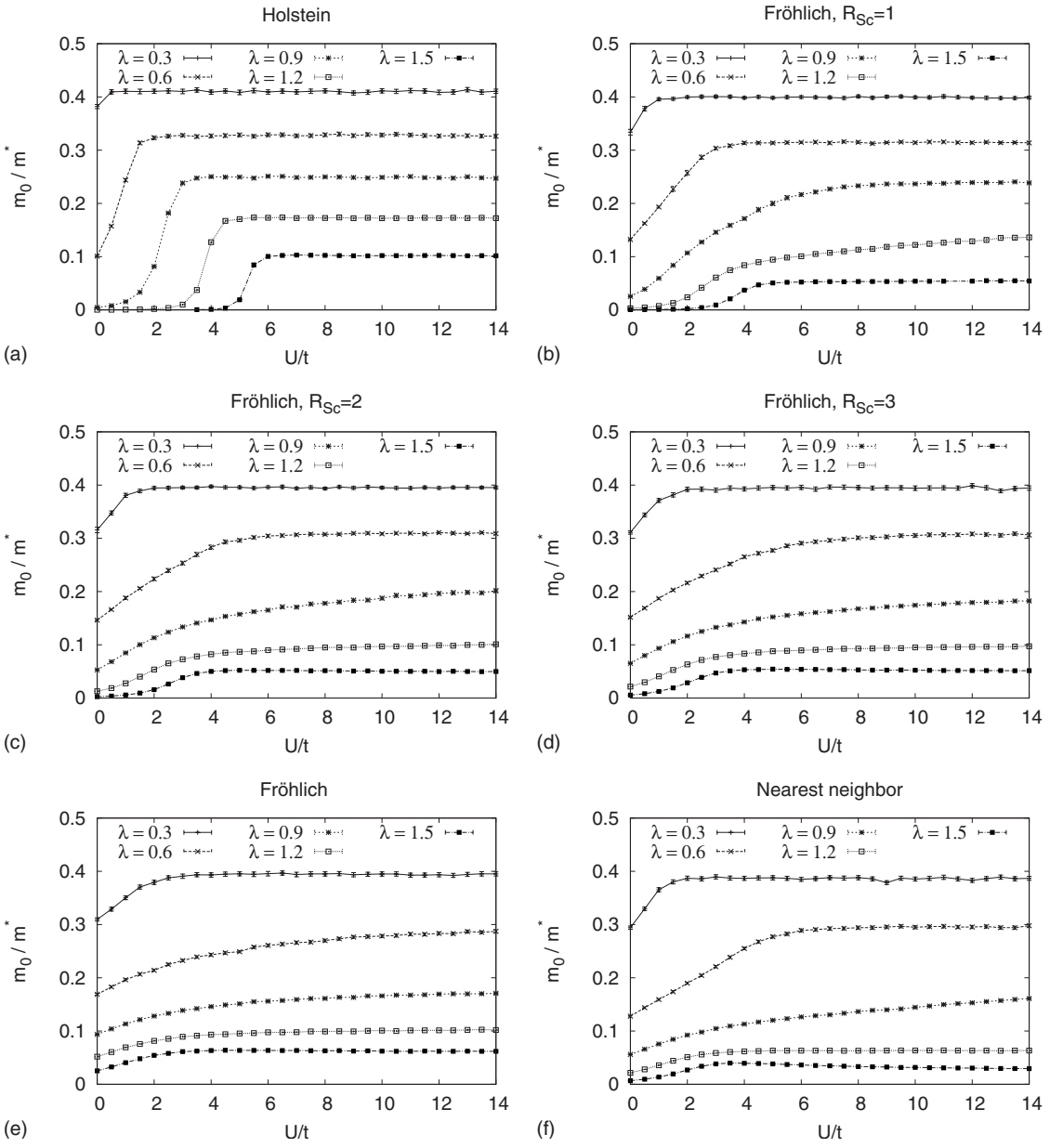

FIG. 4. Inverse mass of the singlet bipolaron. It is clear that both the more complicated lattice-Fröhlich bipolaron and the simplified model with nearest-neighbor interaction generate bipolarons with similar light mass. The inverse mass of the nearest-neighbor model has a small hump around $U=3$.

For completeness, we note that it is also possible to compute properties of the bipolaron at weak coupling and $U>0$, where neither singlet nor triplet bipolarons are bound, i.e., the measured properties correspond to those of two polarons. The weak-coupling properties of the polaron can be determined from second-order perturbation theory and are found to be $E/t=-z-\lambda\Gamma_E(\bar{\omega})$, $m_0/m^*=1-\lambda\Gamma_{m^*}(\bar{\omega})$, $\alpha_{m^*}=\lambda\Gamma_{\alpha_{m^*}}(\bar{\omega})$, and $N_{\mathrm{ph}}=\lambda\Gamma_{N_{\mathrm{ph}}}(\bar{\omega})$. For $\bar{\omega}=1$, the Γ coefficients can be found in Ref. 24, with the exception of the coefficients for the nearest-neighbor model which are $\Gamma_E=2.391(5)$, $\Gamma_{m^*}=0.607(7)$, $\Gamma_{\alpha_{m^*}}=0.294(1)$, and $\Gamma_{N_{\mathrm{ph}}}=1.999(1)$ and for the Hubbard-Fröhlich model with $R_{sc}=2$, which are $\Gamma_E=1.423(7)$, $\Gamma_{m^*}=0.392(0)$, $\Gamma_{\alpha_{m^*}}=0.1540(0)$, and $\Gamma_{N_{\mathrm{ph}}}=1.116(2)$.

IV. TRIPLET BIPOLARONS IN THE HUBBARD-FRÖHLICH MODEL

In this section, we compute the properties of triplet bipolarons and compare with those of singlet bipolarons. Our algorithm can compute triplet and singlet properties simultaneously since they are related through the measurement of the exchange sign. Strictly, it is not necessary to directly calculate the properties of triplet states in 1D in this way (singlet and triplet bipolarons are degenerate at large U) however this contributes part of the development of our algorithm since there is no alternative approach for two dimensions and above. The Hubbard-Holstein model in 1D has no bound triplet states, so the properties associated with triplet symmetries are not examined for local interactions.

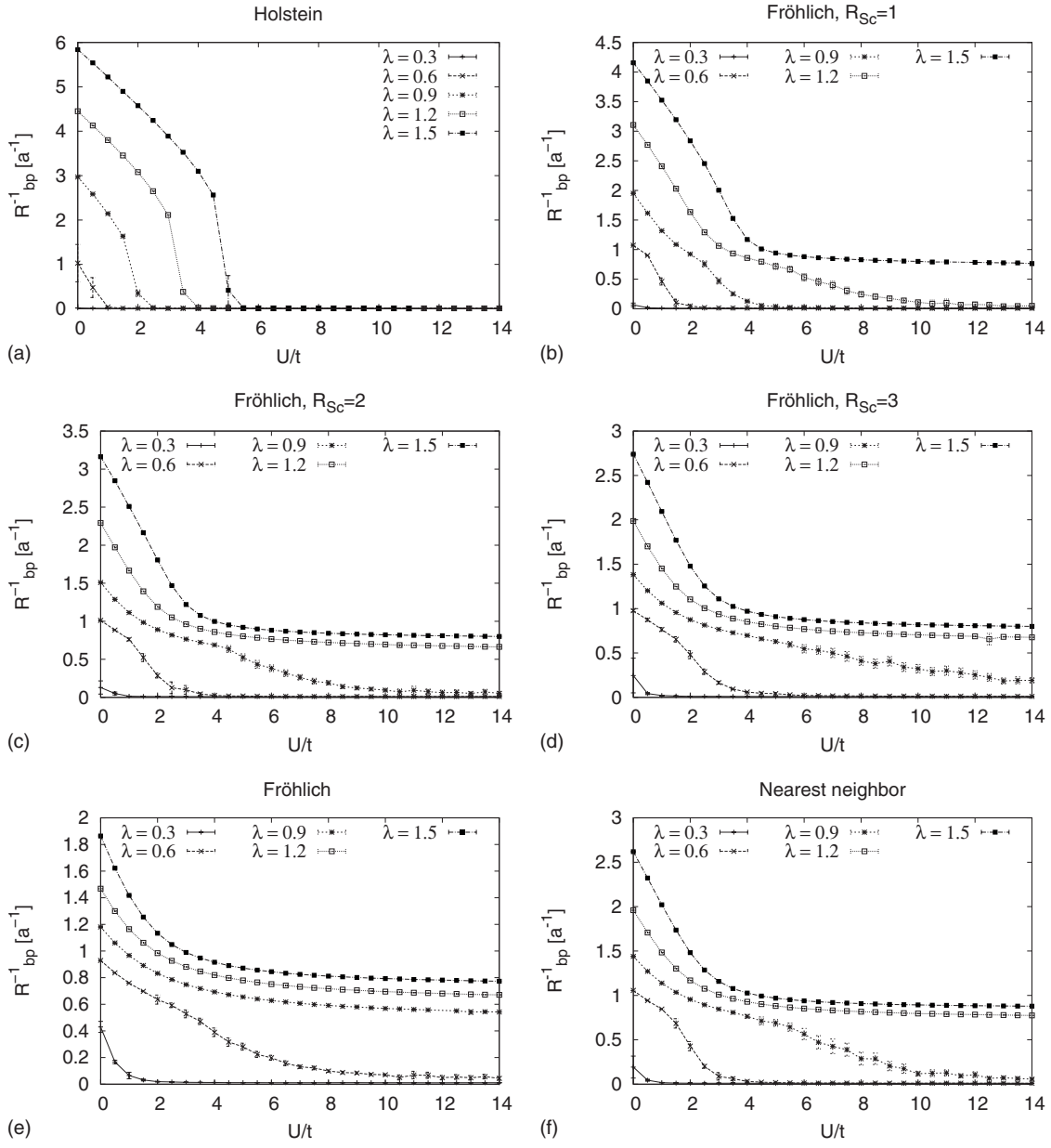

FIG. 5. Inverse pair size associated with the singlet bipolaron. The Holstein bipolaron always breaks up at large U, indicated by the vanishing inverse radius. In contrast, all the models with long-range interaction have bound S1 states at large U when there is sufficient electron-phonon coupling.

A quantity that is straightforward to measure using our Monte Carlo algorithm is the energy splitting between singlet and triplet bipolaron states. From this and the singlet energy, the total energy of triplet bipolarons can be determined. The singlet-triplet splitting and singlet and triplet energies are shown in Fig. 7. Figure 7(a) shows the total singlet and triplet energies for various λ, $\bar{\omega}=2$, and $U=14$. Below a certain electron-phonon coupling, the singlets and triplets are degenerate, as Coulomb repulsion inhibits pairing in the singlet, and the triplet state (which must be higher in energy than the singlet) is unbound. This can also be seen for $\omega/t=4$ and $U/t=14$. The singlet-triplet splitting is relatively small compared to the total energy of the bipolaron and the total energy only changes slightly on increase in phonon frequency.

Figure 7(b) shows the splitting between singlet and triplet states for a variety of U/t and λ. On decreasing U, the singlet-triplet splitting increases. This is expected as the singlet state becomes increasingly well bound on decreasing U, whereas the binding energy of the triplet should remain constant. Efficient computation of the splitting is limited by the temperature, as the higher energy triplet configurations need to be visited enough to obtain accurate statistics. For the $\bar{\beta}=7$ shown here, this effectively limits us to maximum splittings of the order of $t/2$ (otherwise computation time is excessive). Increase in λ also increases the splitting, which can also be seen in Fig. 7(a).

We also examine the relative masses of the triplet and singlet bipolarons, which can be seen in Fig. 8. We begin by computing the inverse effective mass for $\bar{\omega}=2$, $U/t=14$, and

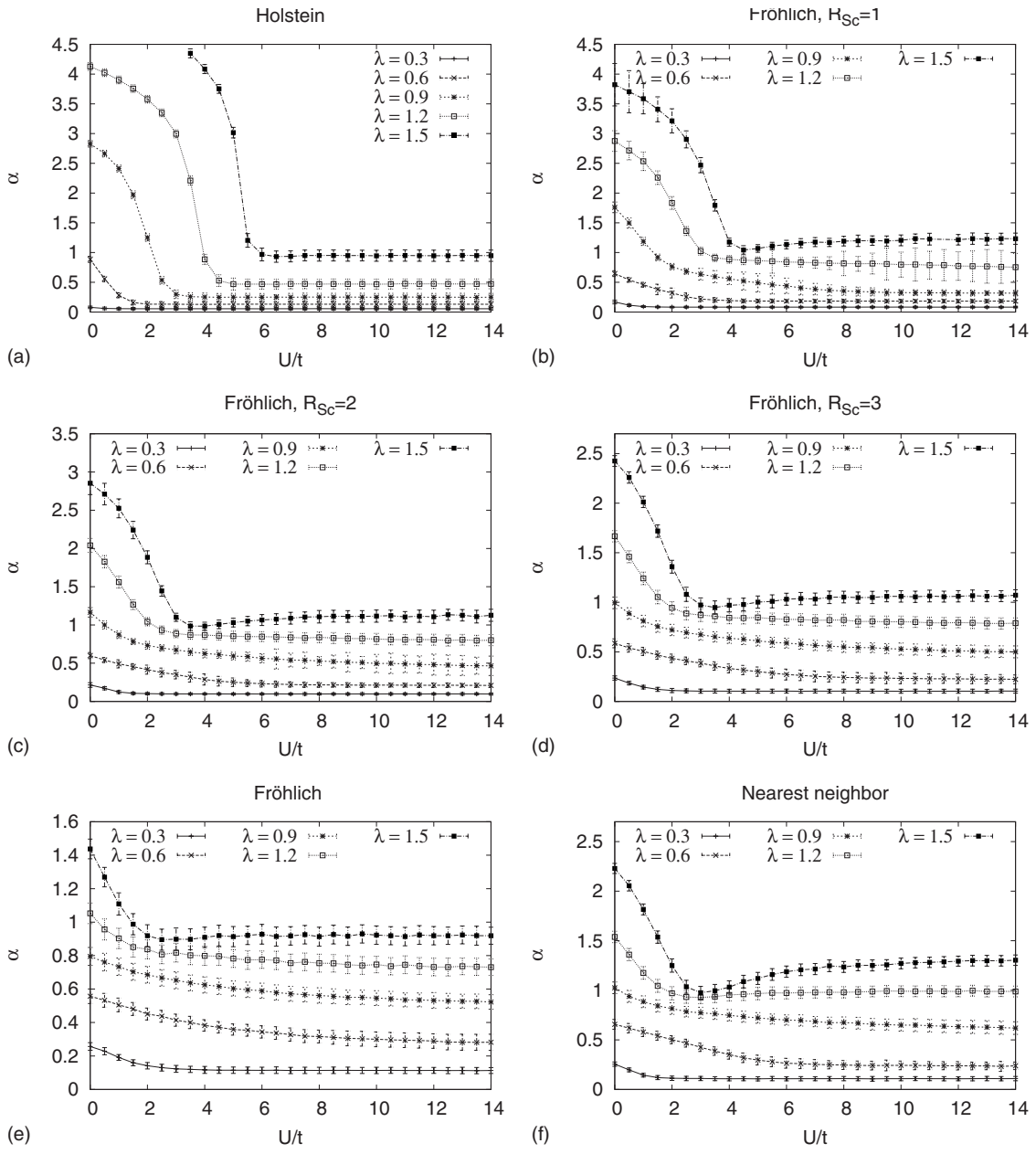

FIG. 6. Mass isotope exponent of the singlet bipolaron. The dip in the exponent seen in the models with long-range interaction corresponds to the crossover between S0 to S1 bipolarons. In general, the mass isotope exponent is much larger for S0 pairs (low U) than S1 pairs (high U, λ, and long-range interactions).

$\bar{\beta}$=7 which can be seen in Fig. 8(a). For large λ, it is clear that the triplet bipolaron is heavier than the singlet one. However, for small λ, the situation is reversed, with the triplet state slightly lighter than the singlet one. The slightly lighter mass is persistent to λ ~ 1.125, where the masses cross, for large λ, triplets are observed to be heavier than singlets. We also make computations for U/t=14 and $\bar{\omega}$=4. Triplets are heavier than singlets over a wider range of the parameter space for larger ω. This is consistent with the large ω limit, where the models with long-range interaction have similar properties to the UV model (the UV model always has heavier triplets).

Figure 8(b) shows how the masses of singlets and triplets change with U. On decreasing from large U, the singlet mass decreases to become lighter than the triplet as the S0 and S1 states become degenerate. However at small U this is reversed since the singlet becomes tightly bound in an S0 state (see Fig. 2). This binding into an S0 state and the associated increase in mass can also be seen in the λ=0.5 curves at low U.

The number of phonons associated with singlet and triplet bipolarons is shown in Fig. 9 with the difference between them shown in the inset. Simulations were run for $\bar{\beta}$=7, $\bar{\omega}$=2, U=14t, and various λ. The number of phonons associated with singlet and triplet bipolarons is very similar. For the parameters shown, there are slightly more phonons associated with the singlet than the triplet but the number of phonons is degenerate when λ is very small (as the two

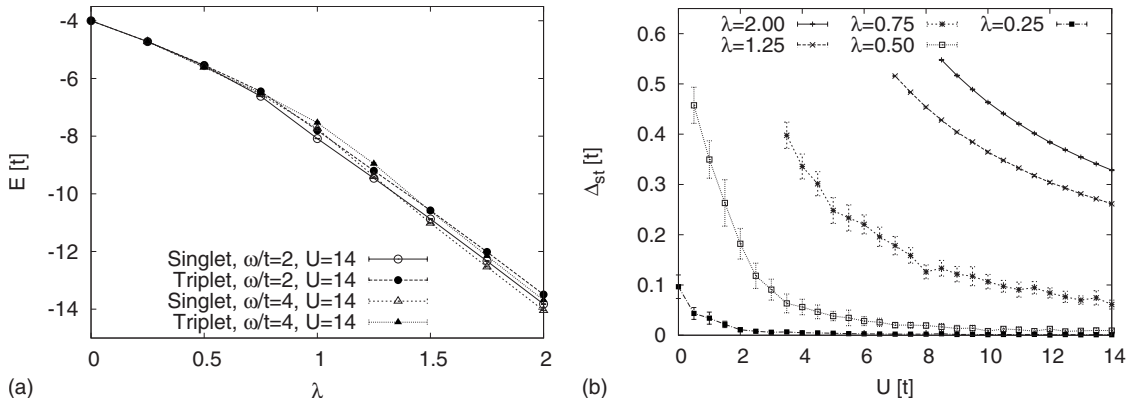

FIG. 7. (a) Total triplet and singlet energies of Hubbard-Fröhlich bipolarons. $U=14t$, $\bar{\beta}=7$, $\bar{\omega}=2$ and $U/t=14$, $\omega/t=4$, $\bar{\beta}=7$. (b) Singlet-triplet splitting when $\bar{\beta}=7$, $\bar{\omega}=2$, and various U/t and λ.

particles are not bound). The number of phonons associated with the cloud is also similar for singlet and triplet bipolarons at very large λ. For such a large U and $\lambda=2$, the singlet bipolaron has some S1 characteristics which explains the similarity between singlet and triplet. For much larger $\lambda \gg U/t$, the electron-phonon coupling is expected to overcome the Coulomb repulsion to bind the singlet bipolaron into an S0 configuration and the properties of singlet and triplet will differ.

We complete this section by considering the inverse size of singlet and triplet bipolarons which can be seen in Fig. 10. As before, $\bar{\beta}=7$, $\bar{\omega}=2$, and $U=14t$. The triplet is larger for all λ. This makes the heavier triplet states slightly counterintuitive because in the case of singlets, larger wave functions tend to be associated with lighter bipolarons.

V. BIPOLARON DISPERSION

One of the powers of our Monte Carlo algorithm is the possibility to compute the dispersions of the bipolaron efficiently. In this section, we discuss spectra computed with our algorithm. The estimator for our spectra is given in Eq. (4). We compute triplet and singlet spectra at the same time.

A. Hubbard-Holstein model

In the Hubbard-Holstein model, triplets are never bound, so we do not compute the dispersion associated with triplet symmetry, concentrating instead on singlets. We show the effects of varying U/t on the dispersion of the Hubbard-Holstein bipolaron for $\lambda=1$ and $\bar{\omega}=1$ in Fig. 11. On decreasing U, the electron-phonon interaction begins to dominate, resulting in strongly bound on-site pairs. This is characterized by a significant decrease in the bandwidth, which is consistent with a large increase in the effective mass. For $U/t \gtrsim 5$, the dispersion does not change significantly on increasing U (the bipolaron is not bound at larger U). This is consistent with the estimate from the large frequency limit of the model, where bipolarons unbind if $U > 4t\lambda$.

Figure 11(b) shows the shape of the dispersion, $\epsilon(k)/\epsilon(\pi)$ as compared to the cosine dispersion associated with the noninteracting limit. The dispersion is skewed away from the cosine and is flatter at larger momenta. The dispersion also becomes shallower at larger U where the bipolaron unbinds into two polarons, demonstrating that the band flattening in bipolarons is significantly larger than in polarons.

The effects of varying ω are shown in Fig. 12. As the phonon frequency is increased, the bipolaron band gets

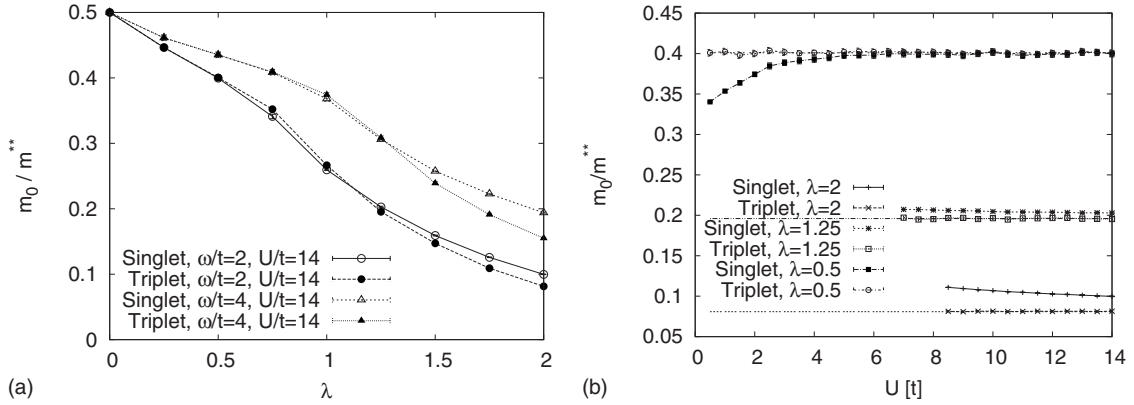

FIG. 8. (a) Inverse mass of singlet and triplet bipolarons when $\bar{\beta}=7$, $\bar{\omega}=2$, and $U=14t$. The Hubbard-Fröhlich model is simulated. N.B. Triplets are heavier than singlets at strong coupling, as in the solution of the UV model. (b) Variation in inverse mass with U. The triplet mass is constant.

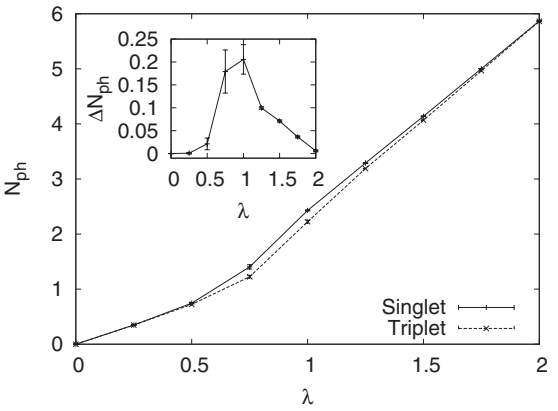

FIG. 9. Number of phonons associated with singlet and triplet bipolarons in the Hubbard-Fröhlich model. Inset: the difference between the number of phonons associated with singlet and triplet bipolarons. These data were computed for the parameters $\bar{\beta}=7$, $\bar{\omega}=2$, and $U=14t$.

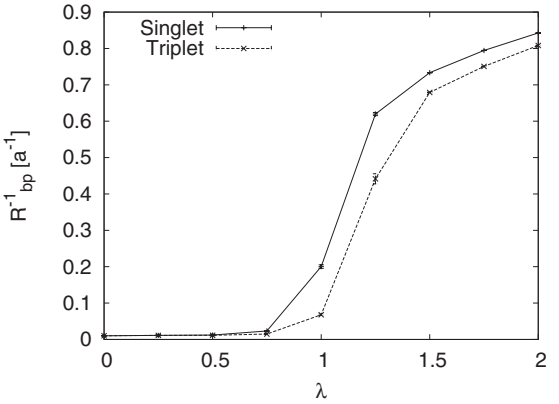

FIG. 10. Inverse size of singlet and triplet bipolarons in the Hubbard-Fröhlich model when $\bar{\beta}=7$, $\bar{\omega}=2$, and $U=14t$.

wider, which is consistent with the decrease in effective mass. The change in bandwidth is quite significant as ω/t changes from 2 to 4 and is around a factor of 10. We also compute the dispersion of the Hubbard-Holstein model for $\omega/t=4$, $U/t=20$, and various λ, which can be seen in Fig. 13. On increased λ, the bandwidth decreases, consistent with the significant increase in effective mass. The bipolaron binds into an S0 state on increasing λ, with the bandwidth changing by more than three orders of magnitude from $\lambda=1$ (not shown in figure) to $\lambda=4$. We note that similar calculations were presented in Ref. 10.

B. Hubbard-Fröhlich model

The form of bipolaron dispersions in the Hubbard-Fröhlich model has not previously been computed. At large coupling and large phonon frequency, the Hubbard-Fröhlich model maps onto a *UV* model, which is a convenient starting point for analytics. The singlet dispersion of the *UV* model can be found from the equation,[22]

$$[\sqrt{\epsilon_s(k)^2 - 16t^2\cos^2(k/2)} + \bar{U}]$$
$$\times[\sqrt{\epsilon_s(k)^2 - 16t^2\cos^2(k/2)} - \epsilon_s(k)] - 2\bar{V}[\bar{U} - \epsilon_s(k)] = 0, \tag{15}$$

the triplet dispersion is given by

$$\epsilon_t(k) = -\bar{V} - \frac{4t^2}{\bar{V}}\cos^2(k/2). \tag{16}$$

Here, we take $\bar{U}=U-2W\lambda$ and $\bar{V}=2W\lambda\phi(\boldsymbol{a})$, which is an acceptable approximation for a very tightly bound state of the Hubbard-Fröhlich model at very large ω (since at very large λ the magnitude of the pair wave function tends to zero too rapidly to sample next-nearest-neighbor interactions).

We plot dispersions for various ω/t with $U/t=20$, $\lambda=8$, $\beta/t=3.5$, and a Fröhlich interaction in Fig. 14. All dispersions are plotted relative to the zone-center singlet energy. We also plot the *UV*-model dispersions on the panel showing the $\omega/t=40$ curves. We have already determined that triplet bipolarons are significantly heavier than singlets in the large *U* large λ regime and this is consistent with the much flatter triplet dispersion. In analytics of the *UV* model,[22] singlet and

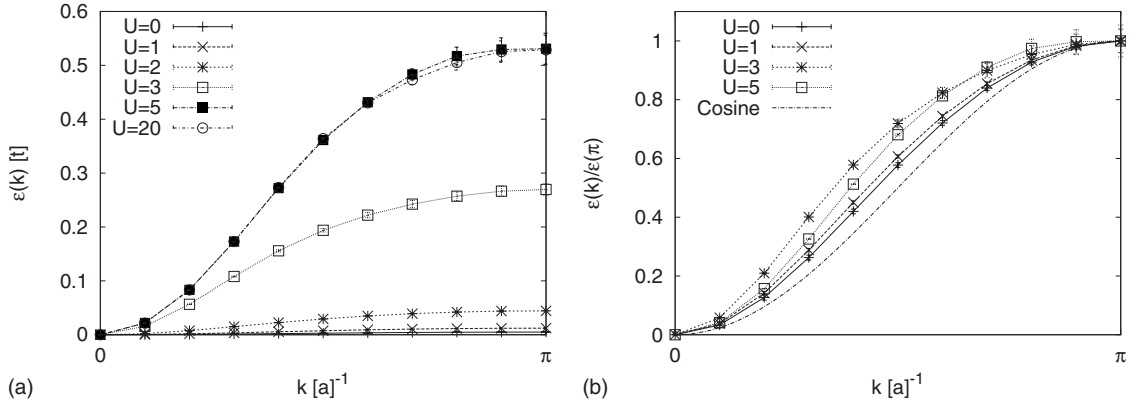

FIG. 11. (a) Dispersion of the Hubbard-Holstein for $\lambda=1$, $\bar{\omega}=1$, $\bar{\beta}=14$, and various *U*. (b) Comparison between the shape of the dispersion, $\epsilon(k)/\epsilon(\pi)$ and the bare cosine band.

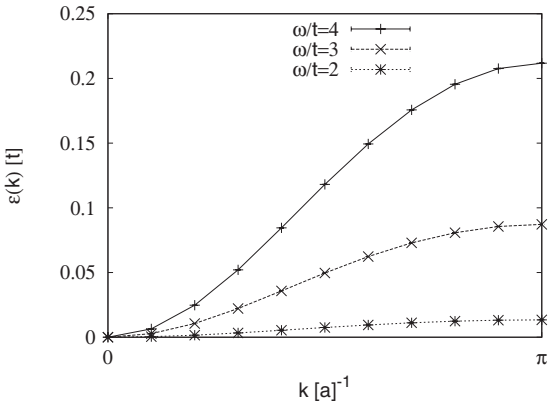

FIG. 12. Dispersion of the Hubbard-Holstein model for $\lambda=2$, $U/t=5$, $\bar{\beta}=7$, and various ω. Error bars are too small to be visible.

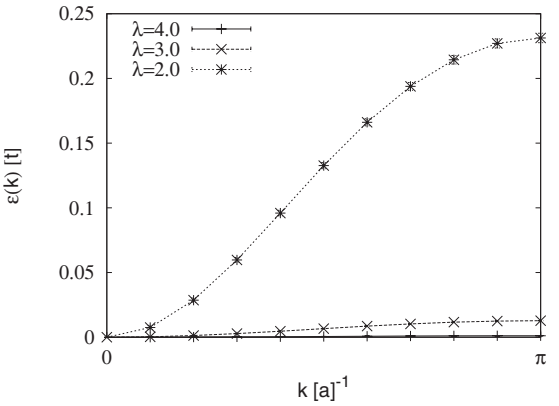

FIG. 13. Dispersion of the Hubbard-Holstein model for $\omega/t=4$, $U/t=5$, $\beta/t=3.5$, and various λ.

triplet dispersions are found to be degenerate at $k=\pi/a$. In agreement with results from the *UV* model, the spectra are nearly degenerate at the zone edge for large phonon frequencies but become increasingly separated in energy for lower phonon frequencies. This is clear evidence that the degeneracy at the π point in the *UV* model is lifted by dynamical effects.

We also investigate the effect of varying λ on the singlet and triplet dispersions in Fig. 15. Data are plotted for the parameters $\omega/t=4$, $\beta/t=3.5$, $U/t=20$, and for various λ. Where no error bars are visible, they are smaller than the points. The dispersions are plotted relative to the zone-center singlet energy. The triplet spectrum is much flatter than the singlet one, which is consistent with the larger triplet masses

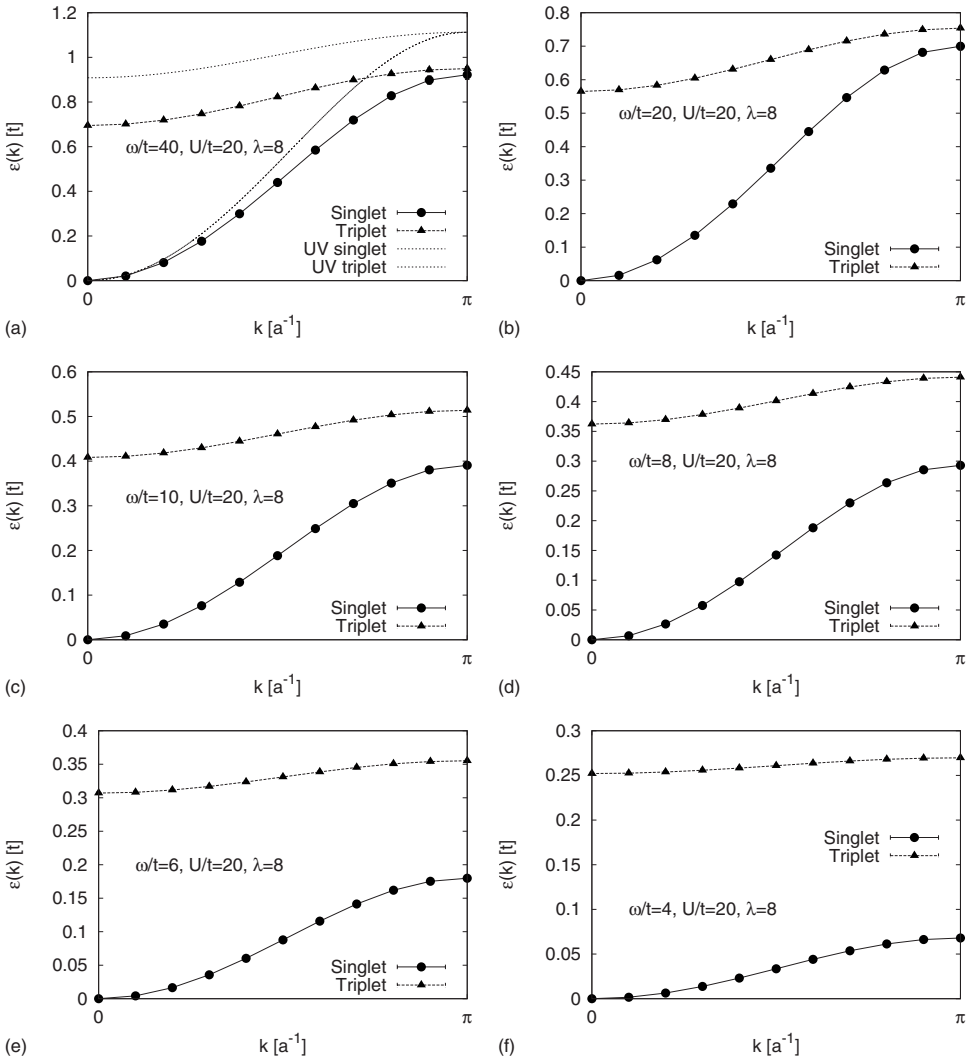

FIG. 14. Singlet and triplet dispersions. Data are shown for various ω/t, $U/t=20$, $\lambda=8$, $\beta/t=3.5$, and a Fröhlich interaction. Error bars are smaller than the points. The dispersions are plotted relative to the zone-center singlet energy. Note that the triplet spectrum is much flatter. The spectra are near degenerate at the zone edge for large phonon frequencies but are separated in energy for lower phonon frequencies indicating that the separation is a dynamical effect. The dispersions of the corresponding *UV* model are also shown on the $\omega/t=40$ plot.

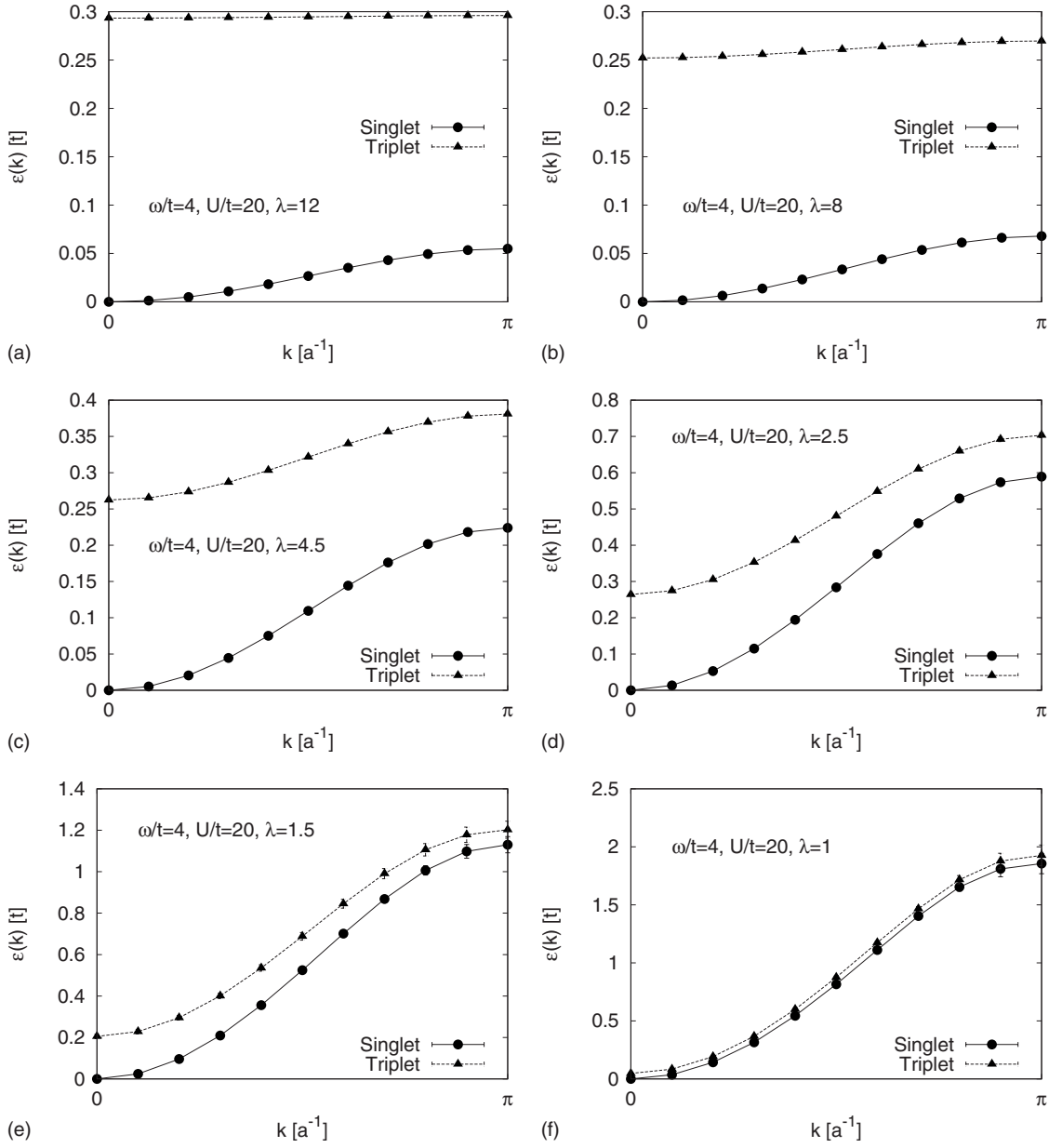

FIG. 15. Singlet and triplet dispersions. Data are plotted for the parameters, $\omega/t=4$, $U/t=20$, various λ, $\beta/t=3.5$, and a Fröhlich interaction. Where no error bars are visible, they are smaller than the points. The dispersions are plotted relative to the zone-center singlet energy. Note that the triplet dispersion is much flatter than the singlet one.

at higher ω and λ. In particular, the triplet dispersion is almost flat for $\lambda=12$ in comparison with the singlet dispersion. For $\lambda=1$, where singlets and triplets are only just bound, the dispersions are near degenerate. In contrast to the Hubbard-Holstein bipolaron, the bandwidth decreases by only one order of magnitude on increasing λ from 1 to 4.5, which is a feature of the long-range interaction.

We are also interested in how the dispersion varies as the Coulomb repulsion is increased. Variation in the singlet spectrum with varying U is shown in Fig. 16. Data are plotted for parameters $\omega/t=4$, $\lambda=2.5$, $\beta=3.5$, and a Fröhlich interaction. The triplet dispersion does not vary with U and as U is increased to very large values singlet and triplet dispersions converge.

In Fig. 17, we compute the zone-center and zone-edge singlet-triplet splitting as ω/t is varied. $\lambda=8$, $U/t=20$, and $\beta=3.5$. As phonon frequency increases, the zone-edge singlet and triplet states become closer in energy with singlet and triplet expected to become degenerate at very large ω as is found in the UV model. Contrary to this, the zone-center singlet-triplet splitting increases with increased ω. This is mainly due to decrease in singlet energy. The triplet also becomes lower in energy on increasing ω but the decrease is smaller than for the singlet bipolaron.

VI. SUMMARY

In this paper, we presented the results of simulations of bipolaron properties for a series of electron-phonon models

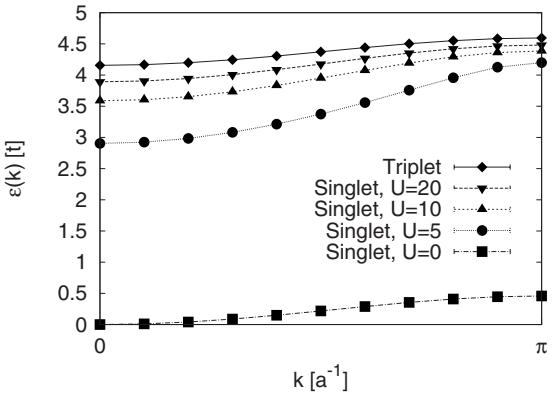

FIG. 16. Variation in singlet spectrum with varying U. Data are plotted for parameters $\omega/t=4$, $\lambda=2.5$, $\beta=3.5$, and a Fröhlich interaction. Error bars are smaller than the points.

in 1D. The models vary in terms of the interaction range, from the simple on-site Holstein interaction, through the model suggested by Bonča and Trugman with interaction only between particles on nearest-neighbor sites to the full lattice Hubbard-Fröhlich model. The continuous-time quantum Monte Carlo algorithm was used to simulate the models and full details of our algorithm have been presented. A wide range of bipolaron properties have been calculated, with a detailed overview of the parameter space and comparison made between models with differing ranges of electron-phonon interaction. In general, only a small long-range interaction is necessary to significantly modify model properties from the strictly local Holstein case, with light masses and strong pairing present for even relatively strong screening.

The strength of the nearest-neighbor effective interaction is found to be the most important factor that influences bipolaron properties. This increases the possibility of engineering a bipolaron condensate in higher dimensions since with shorter tails, clustering corresponding to phase separation is less likely. Naturally, such a condensate would be conditional on a small bipolaron density $n \ll a^3/8R_{bp}^3$, where pair wave functions only weakly overlap. Once bipolaron wave functions overlap significantly the problem becomes complicated, for example, bipolarons could dissociate or there could be a crossover to BCS-type superconductivity. Given that the simplified near-neighbor model is much better suited to analytics than the lattice-Fröhlich approach, it is suggested that it should be adopted as a more general model to investigate electron-phonon problems in higher dimensions. Models involving ions oscillating above the plane or chain of electrons have been suggested to derive this and similar forms. This type of configuration is not possible in three dimensions. However, in $D>2$ a long-range component to electron-phonon models is expected since a perfectly momentum independent interaction is unlikely. Simulation of such models will form part of future publications.

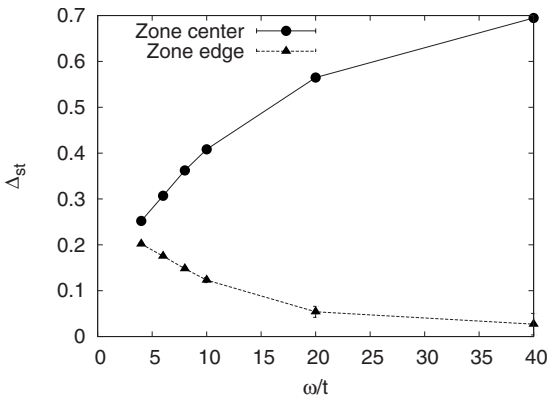

FIG. 17. Dependence of the zone-center and zone-edge singlet-triplet splitting with ω/t. $\lambda=8$, $U/t=20$, and $\beta=3.5$.

ACKNOWLEDGMENTS

We acknowledge useful discussions with John Samson and Sasha Alexandrov.

APPENDIX

The formal derivation of the continuous-time limit for updates (V)–(VIII) by considering detailed balance is very similar to that for updates (I)–(IV), which has been described in detail elsewhere[16] [although here we make a slight modification for weighted insertions, where kinks are more likely to have similar values of τ according to the weighting $p(\tau,\tau')$]. Thus, we simply summarize the rules needed for implementation of the algorithm here. We use only updates I, II, V, and VIII as a minimal update set that allows the algorithm to efficiently explore all path configurations. A detailed derivation is then given for the multiple kink update relating exchanged and direct configurations in Sec. V since there are some subtle considerations.

1. Update (I): Kink addition on both paths

Consider two path configurations C and D, where D has two additional kinks, $\boldsymbol{l}$ on path A and $\boldsymbol{l}$ on path B. The update proceeds by selecting kink shifts, paths, and kinks to add and remove according to the scheme, (i) choose kink-type shifts and paths according to the probability rules R1–R3. (ii) Propose pair removal with probability 1/2. Otherwise attempt pair addition. (iii) If $N_{Al}=0$ or $N_{Bl}=0$ in the initial configuration and pair removal was proposed, then the update is rejected. (iv) For pair addition, select times with equal probability density according to rules R4 and R5. (v) For pair removal, select an $\boldsymbol{l}$ kink from path A and a $\boldsymbol{l}$ kink from path B according to rules R6 and R7,

$$P(\text{addition}) = \min\left\{1, \frac{t^2\beta e^{A(D)-A(C)}}{N_{IA}(D)\sum_{i=1}^{N_{IB}(D)} p(\tau,\tau_i)}\right\}. \quad \text{(A1)}$$

2. Update (II): Addition of kink and antikink pair on one path

Consider two path configurations C and D that differ only in that D has additional kinks $\boldsymbol{l}$ on path A and $-\boldsymbol{l}$ on path A. Using the following rules: (i) choose kink types shifts and the path according to the probability rules R1–R3. (ii) Pro-

pose pair removal with probability 1/2. Otherwise attempt pair addition. (iii) If $N_{Al}=0$ or $N_{A-l}=0$ in the initial configuration and removal was proposed, then reject the update. (iv) For pair addition, select times with probability density according to rules R4 and R5. (v) For pair removal, select an $\boldsymbol{l}$ kink from path A and a $-\boldsymbol{l}$ kink from path A according to rules R6 and R7,

$$P(\text{addition}) = \min\left\{1, \frac{t^2\beta e^{A(D)-A(C)}}{N_{IA}(D)\sum_{i=1}^{N_{-IA}(D)} p(\tau,\tau_i)}\right\}. \quad \text{(A2)}$$

3. Update (V): Addition of kink and antikink on different paths

Consider two path configurations C and D that differ only in that D has an additional hop $\boldsymbol{l}$ on path A and $-\boldsymbol{l}$ on path B. Using the following rules: (i) choose kink types shifts and paths according to the probability rules R1–R3. (ii) Propose pair removal with probability 1/2. Otherwise attempt pair addition. (iii) If removal is chosen and $N_{Al}=0$ or $N_{B-l}=0$ in the initial configuration then removal is aborted as a rejection. (iv) For pair addition, select times with equal probability density according to rules R4 and R5. (v) For pair removal, select an $\boldsymbol{l}$ kink from path A and a $-\boldsymbol{l}$ kink from path B according to rule R6,

$$P(C\to D) = \min\left\{1, \frac{t^2\beta e^{A(D)-A(C)}}{N_{IA}(D)\sum_{i=1}^{N_{-IB}(D)} p(\tau,\tau_i)}\right\}. \quad \text{(A3)}$$

4. Update (VIII): Addition/removal of kink pair to a single path

Consider two configurations C and D, where configuration D has two more kinks on path A than configuration C and the same number of kinks on path B. There is a slight complication here because there are two ways of inserting kinks to reach the end configuration, so we always use equal-time probabilities on this update (i.e., no weighted kink insertions).

(i) Choose kink types shifts and paths according to the probability rules R1–R3. (ii) Propose pair removal with probability 1/2. Otherwise attempt pair addition. (iii) If $N_{Al}<2$ and removal has been chosen, the update is aborted. (iv) For pair addition, select times with equal probability density according to rule R4. We do not correlate kink times on this update due to ambiguities with kink insertion ordering. (v) For pair removal, select two different $\boldsymbol{l}$ kinks from path A.

If the Metropolis scheme is used,

$$P(C\to D) = \min\left\{1, \frac{t^2\beta^2}{(N_l(D)+1)N_l(D)} e^{A(D)-A(C)}\right\}. \quad \text{(A4)}$$

5. Exchange by kink insertion and removal

In the path-integral formalism, an exchange of particles corresponds to swapping the ends of the paths at $\tau=\beta$. An example of an exchanged configuration is shown in Fig. 1. To make the exchange, the $\tau=\beta$ end of path B is shifted by $-\Delta$ lattice sites and that of path A through $+\Delta$ sites. From here on, we refer to the $\tau=\beta$ end of a path as the "top" of the path. This section explains how to take the continuous-time limit of this more complicated class of update.

In the conventional way, update probabilities are determined from the detailed balance equation,

$$W(C)\cdot Q(\text{forward})\cdot P(C\to D) = W(D)\cdot Q(\text{inverse})\cdot P(D\to C), \quad \text{(A5)}$$

where $W(I)$ represents the statistical weight of configuration I and Q is the probability of selecting a specific update from all the available updates (for example, a specific hop direction is chosen and a value for the number of antikinks to remove). Configuration D is the exchanged configuration and C represents the nonexchanged configuration.

The total difference in hopping quanta between initial and final configurations is $\Delta-2m$ since $n=\Delta-m$ kinks are added and m antikinks are removed. Therefore, the ratio of statistical weights in the partition function is

$$\frac{W(D)}{W(C)} = (t\Delta\tau)^{\Delta-2m} e^{A_A(D)-A_A(C)}, \quad \text{(A6)}$$

where the subscript A indicates that only path A is considered for now.

One way of making the $+\Delta$ shift at the top of path A is to insert $\Delta-m$ kinks and to remove m antikinks. The maximum number of antikinks that can be removed is $m=N_{A-l}$ if $\Delta>N_{A-l}$ (since it is not possible to remove more antikinks than exist) or $m=\Delta$ otherwise. The minimum number of antikinks that can be removed is $m=0$. Therefore, there are N_P possible choices of m, where $N_P=\Delta+1$ if $\Delta\le N_{A-l}$, otherwise $N_P=N_{A-l}+1$. It is convenient to write the number of possible updates as the single expression,

$$N_P = \min(N_{A-l},\Delta)+1. \quad \text{(A7)}$$

The value of m is chosen with equal weighting $1/N_P$.

Now that a value of m has been chosen, it is necessary to determine the probability that specific kinks are inserted into or removed from a specific configuration. The probability of removing m of the available N_{A-l} antikinks is simply $1/{}_{N_{A-l}}C_m$. The probability of choosing to introduce $n=\Delta-m$ kinks into configuration C with equal weighting $1/\beta$ is $(\Delta-m)!(\Delta\tau/\beta)^{\Delta-m}$ (the probability is increased because there are $(\Delta-m)!$ possible ways to order the kink insertion that are not distinguishable in the final configuration).

All of these considerations contribute to the probability of updating from configurations C to D via the product,

$$Q(\text{forward}) = \frac{(\Delta-m)!}{\min(N_{A-l},\Delta)+1}\left(\frac{\Delta\tau}{\beta}\right)^{\Delta-m}\frac{1}{N_{A-l}C_m}. \quad \text{(A8)}$$

The inverse process changes the path from configuration D to C. Similar to the forward process, up to Δ kinks can be removed if they exist, otherwise, only $N_{Al}+\Delta-m=N_{Al}+n$ kinks may be removed. Therefore there are $N_P=\min(N_{Al}+n,\Delta)+1$ possible ways to choose how many kinks to remove. In the reciprocal process, m antikinks are

inserted and $\Delta-m$ kinks are removed from $N_{AI}+\Delta-m$ kinks, so the total probability for choosing a specific inverse process is

$$Q(\text{inverse}) = \frac{m!}{\min(N_{AI}+n,\Delta)+1}\left(\frac{\Delta\tau}{\beta}\right)^m \frac{1}{N_{AI+\Delta-m}C_{\Delta-m}}. \tag{A9}$$

Substituting these probabilities into the detailed balance equation, it is possible to write the ratio update probabilities for a single path as

$$\frac{P_A(C\to D)}{P_A(D\to C)} = \exp[A(D)-A(C)]\frac{m!}{(\Delta-m)!} \times \frac{\min(N_{A-I},\Delta)+1}{\min(N_{AI}+n,\Delta)+1}\left(\frac{\Delta\tau}{\beta}\right)^{2m-\Delta} \times (t\Delta\tau)^{\Delta-2m}\frac{N_{A-I}C_m}{N_{AI+\Delta-m}C_{\Delta-m}}. \tag{A10}$$

There is a cancellation of the discrete time interval $\Delta\tau$, so the continuous-time limit can be taken immediately,

$$\frac{P_A(C\to D)}{P_A(D\to C)} = \exp[A(D)-A(C)] \times (t\beta)^{2n-\Delta}\frac{\min(N_{A-I},\Delta)+1}{\min(N_{AI}+n,\Delta)+1}\frac{N_{A-I}P_{\Delta-n}}{N_{AI+n}P_n}. \tag{A11}$$

A similar result is obtained for path B with kinks replaced by antikinks and vice versa. The probabilities for the two paths are independent and so the total probability is simply a product of the two. Once the ratio of update probabilities has been calculated, the Metropolis update scheme can be applied to obtain a suitable Monte Carlo procedure. We note that the factorials in this expression are a potential cause of overflow, so we work with logarithms in our code.

6. Common segment exchange

There is another possible exchange type, which involves swapping the allocation of kinks between paths for $\tau > \tau_{CS}$ for any common segment at τ_{CS}, i.e., kinks at times $\tau > \tau_{CS}$ associated with path A are reassigned to path B and those assigned to path B are reassigned to path A (common segment means that the two paths occupy the same lattice site at the same imaginary time). Common segment exchange is not applicable for all path configurations but has potential to speed up computation. In our algorithm, we attempt a common segment exchange with probability p_{CS} every time an exchange is attempted. Once the attempt is started, we test for the existence of a common segment. If there are no shared segments, then the update is rejected and no further exchange is attempted on that time step. Otherwise, the common segment exchange is accepted with probability $P(C\to D)=\min\{1,\exp[A(D)-A(C)]\}$.

7. Path shift

To encourage rapid exploration of the path configurations, it is also convenient to introduce another update that is attempted with a small independent probability relative to the other updates. In this update, one of the paths is shifted by a random number of lattice spacings. These updates are useful when the bipolaron is only just bound. The update proceeds as follows:

Attempt the update with an independent probability on each step. Test the configuration of the paths. If the paths are in an exchanged configuration, then the update is rejected. Otherwise, select one of the paths with equal probability. Choose a displacement for the path at random and choose whether to move the path left or right with equal probability (important for the detailed balance so the move is reversible). The move is accepted with probability $P(C\to D)=\min\{1,\exp[A(D)-A(C)]\}$.

[1] B. J. Kim, H. Koh, E. Rotenberg, S. J. Oh, N. Motoyama, S. Uchida, T. Tohyama, S. Maekawa, Z. X. Shen, and C. Kim, Nat. Phys. **2**, 397 (2006).

[2] L. Perfetti, S. Mitrovic, G. Margaritondo, M. Grioni, L. Forró, L. Degiorgi, and H. Höchst, Phys. Rev. B **66**, 075107 (2002).

[3] *Physics of Organic Semiconductors*, edited by W. Brütting (Wiley-VCH, Weinheim, 2005).

[4] A. Chauvet, S. Paschen, M. N. Bussac, and L. Zuppiroli, Europhys. Lett. **26**, 619 (1994).

[5] L. D. Landau, Phys. Z. Sowjetunion **3**, 664 (1933).

[6] P. E. Kornilovitch, Phys. Rev. Lett. **81**, 5382 (1998).

[7] A. S. Alexandrov and N. F. Mott, Rep. Prog. Phys. **57**, 1197 (1994).

[8] G. Verbist, F. M. Peeters, and J. T. Devreese, Phys. Rev. B **43**, 2712 (1991).

[9] J. P. Hague, P. E. Kornilovitch, J. H. Samson, and A. S. Alexandrov, Phys. Rev. Lett. **98**, 037002 (2007).

[10] M. Hohenadler, M. Aichhorn, and W. von der Linden, Phys. Rev. B **71**, 014302 (2005).

[11] M. Hohenadler and W. von der Linden, Phys. Rev. B **71**, 184309 (2005).

[12] G. Wellein, H. Röder, and H. Fehske, Phys. Rev. B **53**, 9666 (1996).

[13] A. Weiße, H. Fehske, G. Wellein, and A. R. Bishop, Phys. Rev. B **62**, R747 (2000).

[14] J. Bonča, T. Katrašnik, and S. A. Trugman, Phys. Rev. Lett. **84**, 3153 (2000).

[15] J. Bonča and S. A. Trugman, Phys. Rev. B **64**, 094507 (2001).

[16] J. P. Hague, P. E. Kornilovitch, J. H. Samson, and A. S. Alexandrov, J. Phys.: Condens. Matter **19**, 255214 (2007).

[17] A. Weiße, G. Wellein, and H. Fehske, in *High Performance Computing in Science and Engineering '01*, edited by E. Krause and W. Jäger (Springer-Verlag, Berlin, 2002), p. 131.

[18] D. M. Eagles, R. M. Quick, and B. Schauer, Phys. Rev. B **75**,

054305 (2007).
[19] S. El Shawish, J. Bonča, L.-C. Ku, and S. A. Trugman, Phys. Rev. B **67**, 014301 (2003).
[20] A. S. Alexandrov and P. E. Kornilovitch, J. Phys.: Condens. Matter **14**, 5337 (2002); A. S. Alexandrov, Phys. Rev. B **53**, 2863 (1996).
[21] I. G. Lang and Yu. A. Firsov, Sov. Phys. JETP **16**, 1301 (1963).
[22] P. E. Kornilovitch, Phys. Rev. B **69**, 235110 (2004).
[23] P. E. Kornilovitch, in *Polarons and Bipolarons in High-Tc Superconductors and Related Materials*, edited by E. K. H. Salje, A. S. Alexandrov, and W. Y. Liang (Cambridge University Press, Cambridge, England, 1995), Chap. 23, p. 367.
[24] P. E. Spencer, J. H. Samson, P. E. Kornilovitch, and A. S. Alexandrov, Phys. Rev. B **71**, 184310 (2005).